Observation of asymmetric electromagnetic field profiles in chiral metamaterials

Nobuyuki Hisamoto,[1] Tetsuya Ueda,[1,*] Kei Sawada,[2] and Satoshi Tomita[3]

[1]*Department of Electrical Engineering and Electronics, Kyoto Institute of Technology, Matsugasaki, Sakyo-ku, Kyoto 606-8585, Japan*
[2]*RIKEN SPring-8 Center, 1-1-1 Kouto, Sayo, Hyogo 679-5148, Japan*
[3]*Graduate School of Materials Science, Nara Institute of Science and Technology, Ikoma, Nara 630-0192, Japan*

We experimentally observe asymmetric electromagnetic field profiles along two-dimensional chiral metamaterials. The asymmetric field profiles depending on the chirality and the operation frequency have been reproduced well by the numerical simulation. Around a chiral meta-atom, distribution of a Poynting vector is found to be shifted asymmetrically. These results are explained in terms of an analogy with the side-jump mechanism in the electronic anomalous Hall systems.

I. INTRODUCTION

The electromagnetic phenomena such as unidirectional electromagnetic wave propagation have been of much interest. Unidirectional backscattering immune propagation of surface waves, referred to as electromagnetic edge modes, was observed in electromagnetic band gap structures such as photonic crystals [1–3] with topological properties [4,5]. The unidirectional surface wave propagations that appear at the boundary between two different areas with and without broken time-reversal symmetry using ferromagnetic medium [6,7] or broken space-inversion symmetry due to chirality [8–13] are topologically protected and robust against scattering by disorder.

Even in nontopological systems without periodicity, asymmetric propagation of surface plasmon polaritons due to the unidirectional excitation [14–17] has been demonstrated. In these systems, unidirectional wave propagation was observed in various structures with space-inversion symmetry by appropriately setting up incident wave conditions, such as by controlling source positions [14], incident angles [15,16], and the polarization [17]. However, these approaches focused on wave incidence techniques rather than a design of waveguiding structures.

At frequencies far below the electromagnetic band gaps, where the wavelength of propagating waves becomes much longer than the lattice constant, the artificial periodic structures can be regarded as effective media based on the concept of metamaterials [18]. Metamaterials are artificial electromagnetic media which are composed of small elements compared to the wavelength in order to manipulate electromagnetic wave propagation and to discover new electromagnetic phenomena. On the other hand, chirality with broken space-inversion symmetry, such as helices [19,20] or gammadions [21], gives rise to optical activity [22–25], which can rotate a plane of the polarization or may convert linear to circular polarizations and vice versa. Metamaterials with the chirality, referred to as

chiral metamaterials, determine the macroscopic constitutive relations of the effective media including not only permittivity and permeability but also chirality for bi-anisotropic media, by appropriately designing meta-atoms [26–34]. So far, various applications of the chiral metamaterials have been proposed and demonstrated [35–39]. However, little is known about the edgelike mode propagation in the chiral metamaterials at the operation frequencies far below the photonic band gaps due to the Bragg scattering.

In this paper we demonstrate electromagnetic edgelike mode propagation in chiral metamaterials at microwave frequencies. We consider two-dimensional (2D) microwave chiral metamaterials of triangular lattice that are constructed using helical meta-atoms [40,41]. Experimental results show asymmetric magnetic field profiles, which are relevant to edgelike mode propagation in the metamaterials. The field concentration side is switched by inverting the chirality of the meta-atom and by changing the operation frequencies. The asymmetric field profiles are reproduced by numerical simulations based on the finite element method. Furthermore, the numerical simulations visualize asymmetric energy and Poynting vector distribution in the metamaterials, which enables us to understand the behaviors of asymmetric field profiles.

II. EXPERIMENTAL AND NUMERICAL SETUPS

Figure 1 shows schematic illustrations of 2D chiral metamaterials and the calculated dispersion diagram. A right-handed (RH) chiral meta-atom was composed of a metallic-wire RH helix. The chiral axis is along the z direction. As illustrated in Fig. 1(a), design parameters for the meta-atom are as follows: wire diameter $d_w = 0.4$ mm, numbers of turns in the helix $t = 3.5$, pitch of turns $p = 1$ mm, and helix diameter $d_h = 2.4$ mm.

The resonance frequency of the lowest mode for the isolated chiral meta-atom is calculated to be 7.0 GHz, which is determined by the total length of metal wire corresponding to a half wavelength of microwaves. Array of the meta-atoms comprises the 2D chiral metamaterial with thickness of a single meta-atom. Figure 1(c) illustrates the dispersion
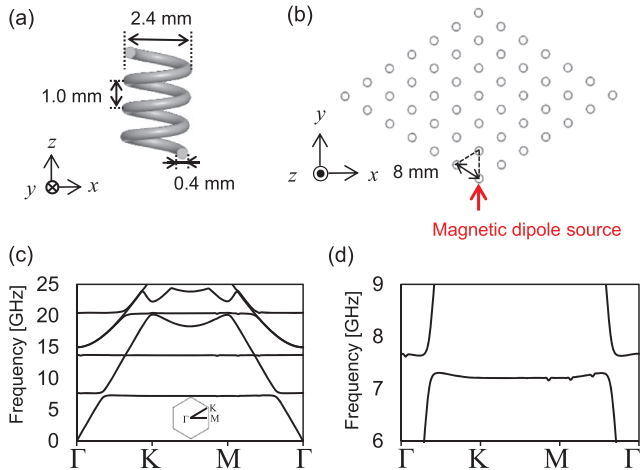
*ueda@kit.ac.jp

FIG. 1. (a) Side view of a RH chiral meta-atom. (b) Top view of a finite rhombus-shaped 2D RH chiral metamaterial with triangular lattice. Red arrow at the bottom indicates the magnetic-dipole excitation position. (c) Dispersion diagram of a 2D RH chiral metamaterial with infinite triangular lattice. (d) The enlarged dispersion diagram in the vicinity of the lowest resonant mode in (c).
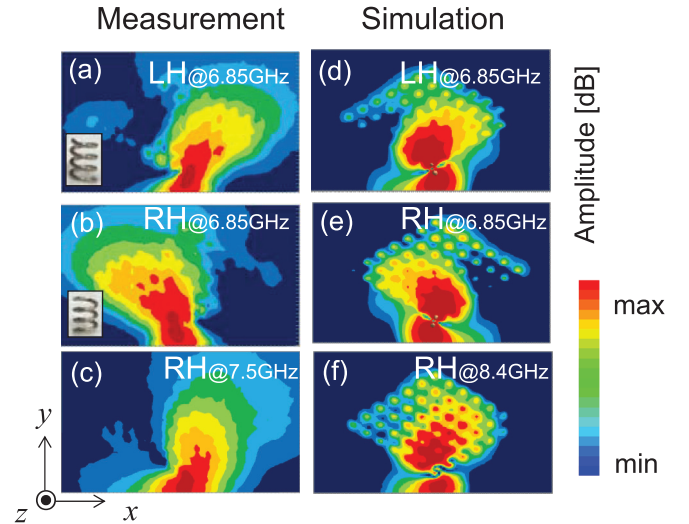

FIG. 2. Measured [(a)–(c)] and simulated [(d)–(f)] profiles for the y component of the magnetic fields. (a) and (d) at 6.85 GHz for the LH chiral metamaterial, (b) and (e) at 6.85 GHz for the RH chiral metamaterial. (c) and (f) also for the RH chiral meta-atoms but at 7.5 and 8.4 GHz, respectively.

diagram calculated for the 2D RH chiral metamaterials consisting of the RH chiral meta-atoms in infinite triangular lattice under the periodic boundary condition. In the numerical simulation setup for the eigenmode analysis, a perfect magnetic conductor (PMC) has been set on top and bottom boundaries of the calculation region, because we are focusing on the TE mode propagation near the lowest-order magnetic dipolelike resonance of chiral meta-atoms. The lattice spacing among the meta-atoms were set to 8 mm.

For the eigenmode calculation, a commercially available electromagnetic field solver based on the finite element method ANSYS HFSS ver. 16 was utilized. Although Fig. 1(c) shows the dispersion diagram of the 2D RH chiral metamaterial, the diagram is independent of the sign of chirality and identical to that of 2D left-handed (LH) chiral metamaterials consisting of the LH chiral meta-atoms. Figure 1(d) shows the enlarged dispersion diagram in the vicinity of the lowest resonant mode in Fig. 1(c). In Fig. 1(d), mutual coupling among neighboring meta-atoms under the magnetic-dipolelike lowest-mode resonance at approximately 7.0 GHz gives rise to a backward-wave mode propagation. In the present case, the passband width of the mode is extremely narrow due to the weak coupling. The coupling between the chiral backward-wave mode and TEM mode in free space results in a narrow gap at approximately 7.2 GHz between the Γ and K points as well as between Γ and M points.

Additionally, Fig. 1(c) shows a band gap due to the Bragg scattering at the K and M points around 20 GHz. We have numerically confirmed that this gap is caused by the meta-atom's chirality. When the meta-atom structure is achiral such as with finite-length straight wire or ring shape, this gap will disappear. It would be interesting to control the dispersion by changing the meta-atom's chirality among RH, LH, and achiral, giving topological states to the electromagnetic waves. However, such a study is out of the scope of this paper, and

will be a future issue. Here we focus our attention on the lowest band at approximately 7.0 GHz where such topological effects are negligibly small.

We experimentally and numerically investigate finite rhombus-shaped 2D chiral metamaterials as shown in Fig. 1(b). The meta-atoms with the chiral axis parallel to the z axis were placed on each grid of the 2D triangular lattice on the x-y plane with 7×7 cells. The meta-atom design is the same as shown in Fig. 1(a). In microwave experiments, RH and LH chiral meta-atoms were made of stainless-steel wires. Forty-nine RH(LH) chiral meta-atoms embedded in a polystyrene foam slab comprise the 2D RH(LH) chiral metamaterials so that the wire top edges are aligned to the $-x$ direction.

In the measurement of microwave field profiles, two identical loop antennas with diameter of 2.4 mm were used; one for a magnetic dipole excitation source and another for a magnetic field detection probe. Both antennas are connected to two ports of a vector network analyzer (Agilent PNA N5224A) through coaxial cables. While the meta-atom at the bottom vertex of the rhombus designated by a red arrow in Fig. 1(b) was excited by the excitation source antenna, magnetic field distribution at the slab top surface was measured by scanning the magnetic field detection probe in the x-y plane at a distance of 1 mm on the opposite side of the excitation. In order to reproduce experimental results by the numerical simulation, a time-varying magnetic dipole moment normal to the lattice is placed as an incident wave source just below the meta-atom at the bottom vertex of a rhombus at a distance of 3 mm.

III. RESULTS AND DISCUSSION

A. Measured and calculated magnetic field profiles

Figure 2 shows the measured and calculated magnitude of the magnetic field distribution for the y component around 7.0 GHz corresponding to the magnetic-dipolelike

lowest-mode resonance frequency of the meta-atoms. Figures 2(a)–2(c) are assigned to measured profiles while Figs. 2(d)–2(f) to corresponding calculated total field including both incident and scatted fields. Figure 2(a) highlights that the magnetic fields measured at 6.85 GHz, which is below the magnetic-dipolelike resonance frequency, are concentrated on the right-hand side in the rhombus-shaped LH chiral metamaterial consisting of LH meta-atoms (as shown in the inset). On the other hand, the fields in the RH chiral metamaterials at the same frequency shown in Fig. 2(b) are concentrated on the left-hand side. These asymmetric field profiles depending on the meta-atom's chirality have been reproduced in the numerical simulation. The calculated magnetic field in the LH chiral metamaterial is concentrated on the right-hand side [Fig. 2(d)], whereas that in the RH chiral metamaterial on the left-hand side [Fig. 2(e)]. Therefore we observed asymmetric magnetic field distributions that are reversible with meta-atom's chirality both in experiments and numerical simulation. It is noted that we still have differences of the magnetic field profiles near the exciting point between the numerical and measurement results. This is due to the fact that the excitation in the numerical simulation is an ideal magnetic dipole while the excitation in the measurement is a loop antenna fed with coaxial cables without symmetry, and in addition, the measured magnetic field profiles were averaged over the cross section of the loop antenna.

Magnetic field distribution is also reversed by elevating the microwave frequency beyond the lowest-mode resonance frequency. Figure 2(c) shows the field distribution in the RH chiral metamaterials measured at 8.4 GHz, which is above the resonance frequency. In Fig. 2(c) the magnetic field concentrates on the right-hand side, which is opposite compared to that at 6.85 GHz [Fig. 2(b)]. We notice a difference between the measured and simulated operation frequencies in Figs. 2(c) and 2(f). The difference is likely to be traced back to the imperfection of the fabricated chiral meta-atoms. Nevertheless, still the asymmetric distribution has been reproduced in the numerical simulation as illustrated in Fig. 2(f). The further experimental and numerical results have revealed that the profiles for the x component of magnetic fields are concentrated on the opposite side to the y component and also inverted by changing the metamaterial chirality and selecting the operation frequency above or below the resonance, although they are not shown here. Additionally, we have confirmed experimentally that electric fields also show similar asymmetric distributions.

B. Calculated energy and Poynting vector distribution

We numerically calculated the electromagnetic energy density $\frac{1}{2}\varepsilon_0|E|^2 + \frac{1}{2}\mu_0|H|^2$ distribution for RH and LH chiral metamaterials at 6.85 GHz. The simulation setups are the same as those in Figs. 2(d)–2(f). In order to highlight the stored energy distribution difference between LH and RH metamaterials, we subtract the energy distribution in the LH chiral metamaterial from that in the RH chiral metamaterial and map the difference in Fig. 3. In this map the red color corresponds to higher energy stored in the RH metamaterial while the blue color corresponds to higher energy stored in the LH metamaterial. We observe in Fig. 3 that the energy in the RH (LH) metamaterial is stored at the left (right) bottom edge.
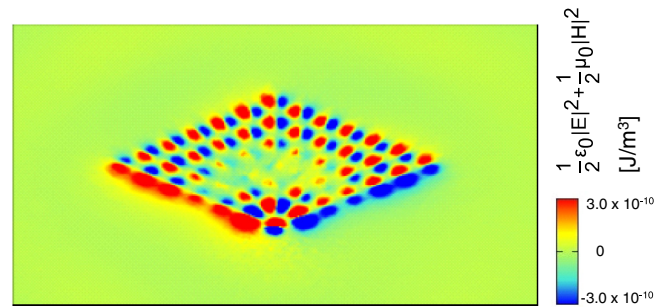

FIG. 3. Calculated energy distribution difference evaluated by subtracting the energy density for LH chiral metamaterial from that RH case at 6.85 GHz. Red and blue colors correspond to the higher stored energy in the RH and LH chiral metamaterials, respectively.

The stored energy clearly shows asymmetric field distributions in the chiral metamaterials.

In order to investigate the transmitted power flow in the 2D chiral metamaterial, Poynting vector distribution was calculated on the slab top surface, since the power density vector cannot be directly observed in the measurement. Figure 4(a) illustrates the calculated distributions of real part of complex Poynting vectors for LH chiral metamaterials at 6.85 GHz. The arrows color corresponds to the Poynting vectors intensity. In Fig. 4(a) the Poynting vector at the excitation point circulates along the helical shape of the meta-atom and the intensity is concentrated on the left-hand side. It is found from Fig. 4(a) that the Poynting vector intensity is asymmetrically distributed around the first-neighbor meta-atoms. In fact, the intensity at the neighboring meta-atom on the right-hand side in Fig. 4(a) is much stronger than those on the left-hand side. The Poynting vector initially directs to the left at the source point, gradually varies with the distance from the origin, rotates in the clockwise direction, and finally flows into the right boundary edge where the field energy is concentrated in the LH chiral metamaterial, as found in Fig. 3. In this way, electromagnetic waves along the LH chiral metamaterial propagate asymmetrically circulating in the clockwise direction, and cause the asymmetric energy distribution concentrating at the right boundary. Contrastingly, as shown in Fig. 4(b), the Poynting vector in the RH chiral metamaterial directs to the right side in the vicinity of the input source. Direction of the Poynting vector rotates in the counterclockwise direction, and results in the vector flow to the left boundary edge where the field energy is concentrated in the RH chiral metamaterial.

Additionally, comparison between the Poynting vector distribution in Fig. 4 and the magnetic field profiles in Fig. 2 makes us realize the fact that the power flow is related to the field profiles. In Fig. 4(a) the Poynting vector is mainly in the y direction on the right-hand side of the metamaterial sample while the vector is in the x direction on the left-hand side. The power flow is governed by the near field magnetic couplings between chiral meta-atoms under the resonance. In other words, the in-plane components of the magnetic field determine the strength and directions of their couplings, i.e., the power flow. Thus the magnetic field for the y component is concentrated on the right-hand side as shown in Fig. 2(a), whereas the x component is concentrated on the left-hand side.
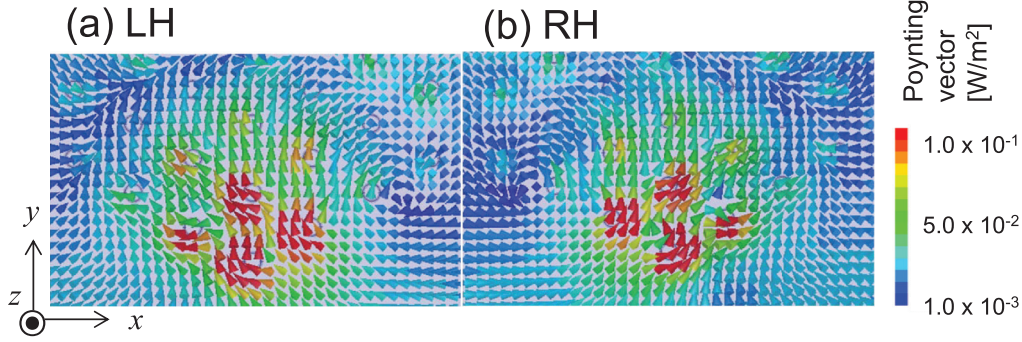
FIG. 4. Calculated Poynting vector distributions at 6.85 GHz in (a) LH and (b) RH chiral metamaterials excited by the magnetic dipole.

In further experiments we have confirmed that the asymmetries of the fields shown in Fig. 2 do not drastically change for cases with chiral meta-atoms having different turn numbers, or with different whole size of the 2D chiral metamaterial. Figures 5(a)–5(c) illustrate the measured magnetic field profiles for two different cases of 2D chiral metamaterials with the helix of 3.5 turns in 15 × 15 cell, 3.5 turns in 7 × 7 cells, and 5.5 turns in 7 × 7 cells, respectively. It is noted that the increase in the size of meta-atoms reduces the resonant frequency, leading to lower operation frequency. In Fig. 5(c) the measured field profile for 5.5 turns is shown at 4.85 GHz that was selected below the reduced resonant frequency of 5.05 GHz. The influence of the total size of 2D chiral metamaterials on the asymmetric field profiles can be confirmed by comparing Figs. 5(a) and 5(b). The influence of number of turns can be found by comparing Figs. 5(b) and 5(c).

Additionally, we numerically investigated the influence of helix orientations around their axis on the asymmetric field profiles by changing the turn number of meta-atoms. In Figs. 5(d)–5(f) magnetic field profiles for the turn number of 3.7, 4.0, and 4.3 are shown, respectively. The corresponding resonant frequencies of meta-atoms were 7.43, 7.10, and 6.82 GHz, respectively. The selected operation frequencies in Figs. 5(d)–5(f) are 6.7, 6.2, and 5.8 GHz, respectively. Overall, all six field profiles in Fig. 5 clearly show the concentration on the left-hand side. Thus, it is confirmed that changes in structural parameters of chiral meta-atoms and in the whole size of metamaterials do not influence significantly asymmetries of the field profiles.

In addition, we note that field profiles on the bottom slab surface show the asymmetries with concentration side opposite to those on the top surface. This exchange of the field asymmetries between top and bottom surfaces is caused by the relation between the geometry of the helical meta-atom and propagation direction along the axis. The electromagnetic waves in the chiral meta-atoms under the resonance are separated into two components: one goes up and the other goes down along the axis of the resonators, and each component behaves differently due to the asymmetric structures. For example, the geometry of the RH helix makes the wave component going up along the structure to rotate in the anticlockwise direction on the top surface, while it forces the other component going down to rotate in the clockwise direction on the bottom surface, respectively.
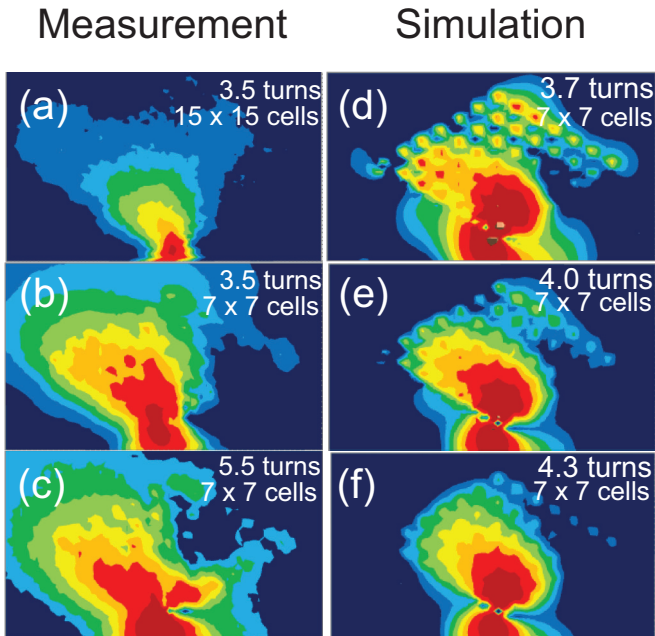
C. Origin of the asymmetric field profiles and energy distribution

Numerical simulation visualized in Fig. 4 shows the asymmetric energy flow in the chiral metamaterials. The energy flow gives rise to asymmetric energy distributions stored in the metamaterials as revealed by the calculation in Fig. 3. The asymmetric energy distribution results in asymmetric magnetic and electric field profiles observed in both experiment and simulation. These asymmetric phenomena of our interest are different from topological effects, because the operation frequency in this study is far below the photonic band gap essential for topologically protected edge modes.

We carried out the further numerical simulation for a scattering problem around a single chiral meta-atom having a 3.5 turn helix with an incidence of plane waves from the

FIG. 5. Measured magnetic field profiles for the *y* component in 2D chiral metamaterial with (a) meta-atoms of 3.5 turns in 15 × 15 cells, (b) 3.5 turns in 7 × 7 cells, and (c) 5.5 turns in 7 × 7 cells. (d)–(f) Simulated magnetic field profiles as a function of the turn number. (d) 3.7 turns at 6.7 GHz, (e) 4.0 turns at 6.2 GHz, and (f) 4.3 turns at 5.8 GHz.
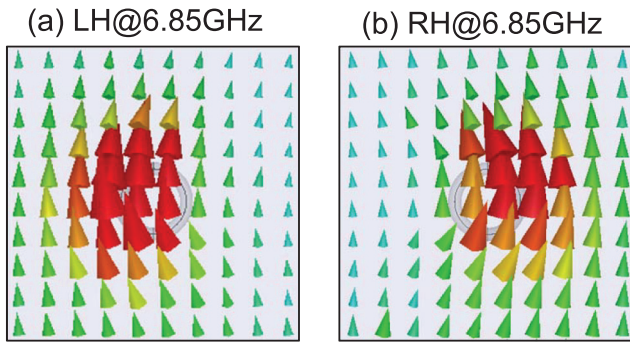
FIG. 6. Calculated Poynting vector distribution at 6.85 GHz for electromagnetic wave scattering around a single (a) LH and (b) RH meta-atom irradiated by plane waves from the bottom.

bottom of Fig. 6, instead of the magnetic dipole excitation. Figures 6(a) and 6(b) show the calculated distribution of a Poynting vector that is observed in the plane with the distance of 1 mm above the top surface of the slab at 6.85 GHz around LH and RH meta-atoms, respectively. The Poynting vector flow around the LH meta-atom in Fig. 6(a) rotates along the helical shape in the clockwise direction, and as a result, the center of the field profiles is transversely displaced on the left-hand side, whereas the center of the power flow around the RH meta-atom is displaced on the right-hand side [Fig. 6(b)]. Thus Fig. 6 provides definitive evidences for asymmetrical selectivity of the electromagnetic wave scattering in the near field region by the chiral meta-atoms. The coupling of these neighboring meta-atoms with asymmetric field profiles in the subwavelength scale leads to the total asymmetric field profiles and energy transfer in the chiral metamaterial. In addition, notably, the Poynting vectors plotted in Fig. 6 are shown to be translated without changing its wave number vectors, and the center of the amplitude is transversely shifted to the one side.

An excited chiral meta-atom in the metamaterials radiates microwaves. The radiated microwaves are scattered by neighboring meta-atoms. A superposition between the radiation and scattering may break a balance between left-handed and right-handed circularly polarized microwaves, resulting in the optical activity by the chiral meta-atom. Based on an analogy between light and electrons, the optical activity in photonic systems corresponds to the spin-orbit interaction in electronic systems [42,43]. Additionally, an electromagnetic Poynting vector represents the velocity of the center of gravity, corresponding to electric currents. Therefore, the Poynting vector flows directed by chiral meta-atoms observed in Fig. 6 is analogous to the electric current flow in an electronic system

with spin-orbit interaction. It is known that such electronic current show skew scattering and side jump by impurities observed in the extrinsic anomalous Hall effects and spin Hall effects for electrons [44–46]. Both mechanisms originate from the spin-orbit interaction in impurity atoms for electrons. While the skew scattering changes the wave number vectors of the electron wave packets, the side jump is a translation of the center of gravity of the packet without changing its wave vectors. Thus the Poynting vector translated without changing its wave number vectors shown in Fig. 6 is analogous to circulating electric current around a scatter with spin-orbit interaction, which is similar to the side-jump mechanism in electronic systems. In the past decade spin-orbit interaction of light in an analogy between light and electrons has been intensively studied in connection with the spin-Hall effect [42,43,47–50]. The present result provides an insight to the understanding of spin-orbit interaction of light. Last but not least, although implemented by microwave meta-atoms, the physical picture unveiled here applies to a broader class of artificial photonic structures in a wide range of frequencies from microwave [51] to visible light [52,53].

IV. CONCLUSIONS

Asymmetric field profiles of electromagnetic waves propagating along 2D chiral metamaterials were observed in both measurements and numerical simulations at frequencies far below the photonic band gap. We found that the field concentrated area was switched both by changing the chirality from LH to RH, or vice versa, and by selecting the operation frequency either above or below the meta-atom's resonant frequency. To understand the mechanism of the asymmetric field profiles, distributions of the energy density and Poynting vector in the chiral metamaterials excited by a magnetic dipole source were numerically investigated. The energy density and the Poynting vector flow were found to be asymmetric. Moreover, for electromagnetic wave scattering from the single chiral meta-atom for incidence of plane waves, the Poynting vector is translated without changing its wave number vectors, and the center of the power flow is transversely displaced on the one side. This is analogous to the side-jump mechanism in the electronic systems with extrinsic anomalous Hall effects. These results pave the way to the realization of the unidirectional surface wave propagation along the chiral metamaterials.

[1] E. Yablonovitch, Phys. Rev. Lett. **58**, 2059 (1987).

[2] S. John, Phys. Rev. Lett. **58**, 2486 (1987).

[3] J. D. Joannopoulous, R. D. Meade, and J. N. Winn, *Photonic Crystals* (Princeton University Press, Princeton, New Jersey, 1995).

[4] F. D. M. Haldane and S. Raghu, Phys. Rev. Lett. **100**, 013904 (2008).

[5] S. Raghu and F. D. M. Haldane, Phys. Rev. A **78**, 033834 (2008).

[6] Z. Wang, Y. D. Chong, J. D. Joannopoulos, and M. Soljačić, Phys. Rev. Lett. **100**, 013905 (2008).

[7] Z. Wang, Y. Chong, J. D. Joannopoulos, and M. Soljačić, Nature (London) **461**, 772 (2009).

[8] A. B. Khanikaev, S. H. Mousavi, W. K. Tse, M. Kargarian, A. H. MacDonald, and G. Shvets, Nat. Mater. **12**, 233 (2013).

[9] L. Lu, L. Fu, J. D. Joannopoulos, and M. Soljačić, Nat. Photon. **7**, 294 (2013).

[10] W. J. Chen, S. J. Jiang, X. D. Chen, B. Zhu, L. Zhou, J. W. Dong, and C. T. Chan, Nat. Commun. **5**, 5782 (2014).

[11] W. Gao, M. Lawrence, B. Yang, F. Liu, F. Fang, B. Béri, J. Li, and S. Zhang, Phys. Rev. Lett. **114**, 037402 (2015).

[12] A. P. Slobozhanyuk, A. N. Poddubny, A. E. Miroshnichenko, P. A. Belov, and Y. S. Kivshar, Phys. Rev. Lett. **114**, 123901 (2015).

[13] L. H. Wu and X. Hu, Phys. Rev. Lett. **114**, 223901 (2015).

[14] I. P. Radko, S. I. Bozhevolnyi, G. Brucoli, L. Martin-Moreno, F. J. Garcia-Vidal, and A. Boltasseva, Opt. Express **17**, 7228 (2009).

[15] H. Kim and B. Lee, Plasmonics **4**, 153 (2009).

[16] X. Li, Q. Tan, B. Bai, and G. Jin, Appl. Phys. Lett. **98**, 251109 (2011).

[17] F. J. Rodriguez-Fortuno, G. Marino, P. Ginzburg, D. O'Connor, A. Martinez, G. A. Wurtz, and A. V. Zayats, Science **340**, 328 (2013).

[18] F. Capolino, *Theory and Phenomena of Metamaterials* (CRC, Boca Raton, FL, 2009).

[19] Z. Y. Zhang and Y. P. Zhao, Appl. Phys. Lett. **90**, 221501 (2007).

[20] Y. Li, R. Ho, and Y. Hung, IEEE Photon. J. **5**, 2700510 (2013).

[21] E. Plum, J. Zhou, J. Dong, V. A. Fedotov, T. Koschny, C. M. Soukoulis, and N. I. Zheludev, Phys. Rev. B **79**, 035407 (2009).

[22] J. C. Bose, Proc. R. Soc. London **63**, 146 (1898).

[23] I. Tinoko and M. Freeman, J. Phys. Chem. **61**, 1196 (1957).

[24] I. Tinoko and R. W. Woody, J. Phys. Chem. **40**, 160 (1964).

[25] D. Moore and I. Tinoko, J. Phys. Chem. **72**, 3396 (1980).

[26] E. J. Post, *Formal Structure of Electromagnetics: General Covariance and Electromagnetics* (North-Holland Publishing Company, Amsterdam, 1962).

[27] F. I. Fedorov, *Theory of Gyrotropy* (Nauka I Technika, Minsk, 1976).

[28] A. Serdyukov, I. Semchenko, S. Tretyakov, and A. Sihvola, *Electromagnetics of Bi-Anisotropic Materials Theory and Application* (Gordon and Breach, Amsterdam, 2001), Vol.11.

[29] S. Tretyakov, I. Nefedov, A. Sihvola, S. Maslovski, and C. Simovski, J. Electromagn. Waves Appl. **17**, 695 (2003).

[30] A. Ishimaru, S. W. Lee, Y. Kuga, and V. Jandhyala, IEEE Trans. Antennas Propag. **51**, 2550 (2003).

[31] J. B. Pendry, Science **306**, 1353 (2004).

[32] S. Tretyakov, A. Sitivola, and L. Jylha, Photon. Nanostruct.-fund. Appl. **3**, 107 (2005).

[33] Y. Jin and S. He, Opt. Express **13**, 4974 (2005).

[34] V. A. Fedotov, P. L. Mladyonov, S. L. Prosvirnin, A. V. Rogacheva, Y. Chen, and N. I. Zheludev, Phys. Rev. Lett. **97**, 167401 (2006).

[35] J. K. Gansel, M. Thiel, M. S. Rill, M. Decker, K. Bade, V. Saile, G. V. Freymann, S. Linden, and M. Wegener, Science **325**, 1513 (2009).

[36] J. K. Gansel, M. Latzel, A. Frolich, J. Kaschke, M. Thiel, and M. Wegener, Appl. Phys. Lett. **100**, 101109 (2012).

[37] J. G. Gibbs, A. G. Mark, S. Eslami, and P. Fischer, Appl. Phys. Lett. **103**, 213101 (2013).

[38] J. Kaschke, L. Blume, L. Wu, M. Thiel, K. Bade, Z. Yang, and M. Wegener, Adv. Opt. Mater. **3**, 1411 (2015).

[39] H. Z. Yao and S. Zhong, IEEE Photon. J. **7**, 4600707 (2015).

[40] S. Tomita, K. Sawada, A. Porokhnyuk, and T. Ueda, Phys. Rev. Lett. **113**, 235501 (2014).

[41] S. Tomita, H. Kurosawa, K. Sawada, and T. Ueda, Phys. Rev. B **95**, 085402 (2017).

[42] F. Jonsson and C. Flytzanis, Phys. Rev. Lett. **97**, 193903 (2006).

[43] C. P. Jisha and A. Alberucci, Opt. Lett. **42**, 419 (2017).

[44] L. Berger, Phys. Rev. B **2**, 4559 (1970).

[45] M. I. Dyakonov and V. I. Perel, Phys. Lett. A **35**, 459 (1971).

[46] S. Onoda, N. Sugimoto, and N. Nagaosa, Phys. Rev. B **77**, 165103 (2008).

[47] M. Onoda, S. Murakami, and N. Nagaosa, Phys. Rev. Lett. **93**, 083901 (2004).

[48] O. Hosten and P. Kwiat, Science **319**, 787 (2008).

[49] K. Y. Bliokh, A. Niv, V. Kleiner, and E. Hasman, Nat. Photon. **2**, 748 (2008).

[50] A. Aiello, N. Lindlein, C. Marquardt, and G. Leuchs, Phys. Rev. Lett. **103**, 100401 (2009).

[51] S. Tomita, K. Sawada, S. Nagai, A. Sanada, N. Hisamoto, and T. Ueda, Phys. Rev. B **96**, 165425 (2017).

[52] L. Marrucci, C. Manzo, and D. Paparo, Phys. Rev. Lett. **96**, 163905 (2006).

[53] O. G. Rodríguez-Herrera, D. Lara, K. Y. Bliokh, E. A. Ostrovskaya, and C. Dainty, Phys. Rev. Lett. **104**, 253601 (2010).